DIPOLAR SONOLUMINESCING MICROBUBBLES

Nick E. Tran

The Tauri Group, 6363 Walker lane, Alexandria VA, 22310

Introduction

Since Fresnel and Schultes first reported the photoemission from the cavitation of microbubbles in 1943 [1], several theories have been proposed to account for the transduction mechanism of microbubble's cavitation into the high-energy photons. It has been conjectured that the observed photoemission is a manifestation of a dynamic Casimir effect due to the zero-point fluctuations of the electromagnetic field during the bubble collapse [2]. However, this theory forbids the emission of UV radiation, and therefore contradicts with the experimental observation [3]. The proton-tunneling radiation theory [4] contests the presence of plasma inside the bubble and postulates that the observed emission is a result of the protons tunneling between the nearly degenerate bound states of water molecule. However, due to the relationship between the tunneling energy barrier (ΔE = 2.9 eV for H_2O) and the spectral peak (λ_{peak}= ch/2ΔE = 213 nm), the theory fails to explain the continuous increase of the spectral intensity from the visible to UV regions of the spectrum [3,5,6].

In this study, we systematically combine the solution chemistry of the microbubble and its cavitation process to form the Dipolar Sonoluminescing Microbubble (DSM) model, which can be summarized as follow. In any microbubble system of solid or liquid where the opposite charges on the bubble's boundary are polarized, under certain conditions, a catastrophic collapse of such a microbubble will produce photons whose intensity and energy are proportional to the charges' concentration and the velocity of their collision, respectively.

Experimental

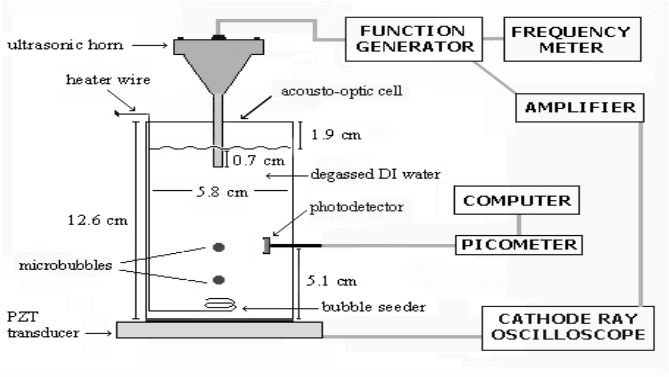

FIG. 1. Schematic representation of experimental arrangement of AO-cell used for generation of microbubble. The vertical acoustic wave field is maintained within the volume of water by two parallel piezoelectric transducers (PZTs). The nichrome bubble seeder wire is attached to a boiler. The position of the UV detector is adjusted during the experiment in order to detect the ultrashort (~1 ns) photoemissions originating from the top bubble. The function generator is set between 26.4-27.6 kHz, corresponding to the resonance frequency of the acousto-optic cell. The operating voltage is 2.5-3.5V

Individual stable bubble could be generated in an acousto-optic (AO) cell (Fig. 1) and then forced to collapse onto the surface of photodiode detectors. Each of photodiode detector adopted for measurement contained a different bandpass filter. The AXUV100LA photodiode included a bandpass filter of 117-131 nm. The highest quantum efficiency (QE_{max} = 85%) of the AXUV100LA photodetector occurs at 124 nm.

Results and Discussion

The integrated signals from the AXUV100LA and AXUV100A1 detectors showed that the cyclic cavitation of microbubble can release 10^6-10^7 photons in the UV and soft-Xray region with irradiance intensities of 1.38 x10^{-6} and 5.08 x10^{-6} Watt/cm^2, respectively. The blackbody radiation curve fit, using Planck energy distribution formula [10]:

$$P_\lambda(\lambda,T) = \frac{8\pi hc^2}{\lambda^5(e^{(hc/\lambda kT)}-1)}$$

showed that the temperature inside the microbubble was around 250,000 ^oC, which is within the temperature range predicted by shockwave models [7,8,9]. This plasma temperature inside the microbubble is in agreement with the estimated temperature derived from thermal bremsstrahlung radiation curve fit [11]:

$$P_{br} \approx g\frac{32\pi}{3^{3/2}}\frac{(2\pi kT)^{1/2}e^6}{m_e^{3/2}c^3h}n_e\sum(n_iZ^2) \qquad (2)$$

where P_{br} is the spectral density and n_e and n_i are taken to be the concentration of protons and anions (6.9x10^{20} m^{-3}) in the DI water, respectively [3].

Dipolar Sonoluminescing Microbubble Model

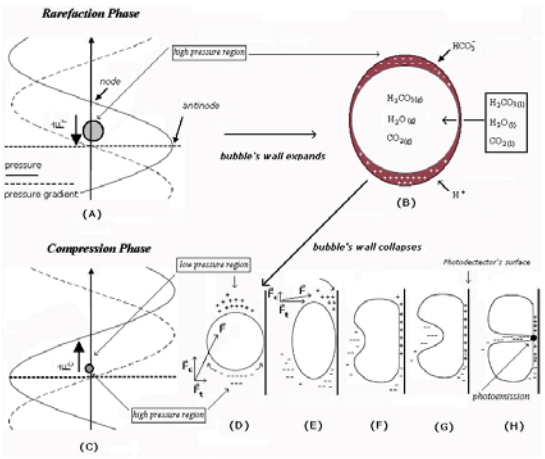

FIG. 2. Proposed DSM model illustrates the progressive events that lead to release of high-energy photons by a hydrated microbubble during its cavitation. The expansion of the bubble's wall (A) during the sound wave's rarefaction phase creates a vacuum inside the bubble, which is then filled as H_2O, H_2CO_3, and CO_2 gaseous molecules were transported across its vacuum-liquid interface (B). As the bubble expands and moves toward the pressure antinode, where the pressure is lowest, H^+ and HCO_3^- ions on the bubble's surface also move in the same direction. The bubble soon becomes dipolar because H^+, being less bulkier and 61 times lighter than HCO_3^-, can move away from the pressure node at a much faster velocity (B). During the compression phase (C), the bubble moves away from the pressure antinode and ions on the bubble's surface reverse their direction, creating aqueous ionic clusters that are in parallel to the compression force field, $\vec{F}_c$ (D). Because of cohesive forces between water molecules on the bubble's surface layer, the bubble continues to maintain a spherical shape until it comes in contact with the solid plane of the photodetector (D). When the bubble begins to lose its spherical symmetry (E), a supersonic microjet of water shoots across the bubble (F-H), carrying with it a net negative charges as it strikes the bubble's wall adhered to the photodiode's solid plane. The collision of the bubble's ionic clusters at supersonic speed results in an electrical microdischarge of high-energy photons.

The plasma temperature inside the microbubble suggests that the observed photoemissions of the microbubble consists primarily of two stages. In the first stage, the high-energy photons generated by the collapse of the microbubble photoionize the anions inside the microbubble [12]. In the second stage, electrons undergo bound-free electronic transition from the anions and accelerated toward the Coulomb field of the protons. The mechanism of the second stage is a well-known phenomenon of thermal bremsstrahlung radiation mentioned above. However, the mechanism of the first stage is still not well-understood and will be explained in terms of proposed DSM model. The model for DI water system used in this study is based on the difference in the ionic mobility of charged species on the microbubble's wall and the formation of water microjet during the microbubble's last compression stage. The mobility of the solvated ions on the bubble's surface is determined by its size as well as the interaction of its solvation shell [i.e, hydronium (H_3O^+), Zundel ($H_5O_2^+$), and Eigen ($H_9O_4^+$)] with the surrounding water molecules. When the microbubble is first nucleated and moves away from the pressure node (Fig. 2A), it eventually grows to a maximum size of 45 μm during the rarefaction phase as charge separation on its surface concurs with the mass transport of H_2O, H_2CO_3, and CO_2 gaseous molecules (Fig. 2B). During the compression phase (Fig. 2C) the bubble moves away from the pressure antinode as it collapses to 1/100 of its maximum size [13] and the ions on the surface of the microbubble reverse their direction (Fig. 2D). During these cycle of rarefaction and compression, which takes 36-38 μsec to complete, the acoustic energy is localized by the sphericality of bubble before it culminates in the observed photoemission event when ionic clusters of opposite charges collide at supersonic speed (Figs. 2E-H). The graphic representations of the hydrodynamics of the bubble collapse near a solid plane in Fig. 2D-F were based on a series of photographs taken by Tomita and Shima [14].

The electrical microdischarge by the collision of the ionic clusters should cause neutral, and singly ionized, nitrogen (λ_{max1} = 5679.56 nm) and oxygen (λ_{max} = 6158.18 nm) gas to emit spectral lines of wavelengths in the visible region. The absence of these spectral peaks in the visible region [5, 13] indicated the concentrations of these gases inside the microbubble are below the detection level. However the absence of the hydrogen atom's emission lines in visible region cannot be explained at the moment (λ_{max} = 6562.85 nm, hydrogen also emits several spectral lines in the 78.06-171.35 nm UV region [16]). However, this absence hydrogen atom's emission lines is probably not due to the extremely short duration of the microbubble's photoemission ($5.0x10^{-11}$ sec., which is 100 times shorter than the shortest lifetime of an excited state of a hydrogen atom in the visible region) as previously suggested by Baber *et al.* [2].

The DSM model can be applied to explain photoemission phenomena in: (1) aqueous and non-aqueous solutions of metal salts, which show that the concentration of ions is a function of photoemission intensity [15] (2) non-aqueous solution where there is there is a difference in mobility between cations and anions, e.g., $Cr(CO)_6$ in octanol and dodecane solutions [16] (3) polar organic solvents exposed to air, e.g., formamide (H_2NCHO), etc. [17] (4) ionic liquids such as butylmethylimidazolium chloride (BuMeImCl), etc. [18] (5) concentrated acid solutions such as H_2SO_4 [19] and (6) ionic systems that facilitate the formation of stable microbubbles.

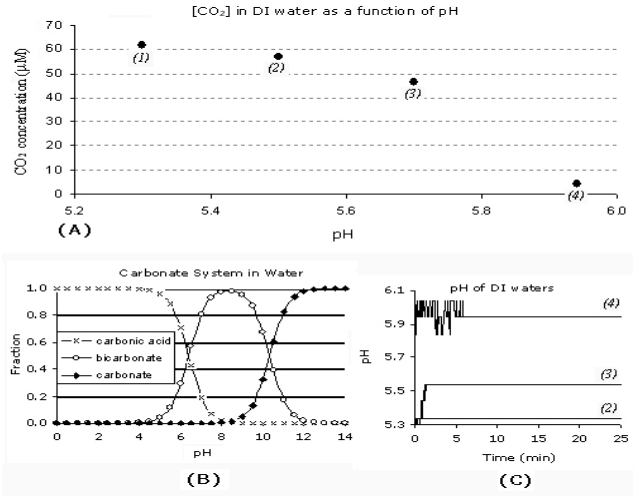

FIG. 3. Carbonate system in different samples of DI water. Sample A1 is fresh DI water. All other samples (A2, A3, and A4) were aliquots taken from sample A1 (18.2 Mω.cm). Graph A show the effectiveness of several methods employed to removal CO_2 from DI water: A2 was heated to boil in a microwave oven for 10 min., A3 was heated to boil over a hot plate for 60 min., and A4 was degassed under vacuum in a hot water bath for 10 min., and then cooled in an ice bath for 1 hr. The pH and carbonate concentration for all the samples were measured at 23°C. Sample A4, which was used to generate microbubbles, has the lowest concentration of CO_2 51.9 μM) and highest pH of all the samples taken. Figure B shows the fractions of H_2CO_3, HCO_3^+, and CO_3^{-2} at various pHs based on their equilibrium coefficients. Figure C shows the pH measurements of C2, C3, and C4; these were the same samples as A2, A3, and A4, respectively. The pH of A1 was 5.3, not shown.

Conclusions

The persistent presence of carbonates in the DI water (Fig. 3) suggests that protons and its high mobility compared to their counter ions, HCO_3^-, can polarize the surface of the microbubble during its rarefaction and compression phase. The polarization of charged species on the microbubble's surface coupled with the formation of water microjet during the microbubble's last compression stage are proposed as the mechanism of the microbubble's photoemission. The intensity and the energy of the photons produced by the cavitation of the microbubble are proportional to the charges' concentration on the microbubble's surface and the velocity of their collision, respectively. The DSM model suggests that the damage done by cavitation of microbubbles to a metal surface in water might be mitigated if correct excess charges are applied to that surface.

REFERENCES:

[1] H. Frenzel and H. Schultes, Z. Phys. Chem. **B27**, 421 (1934).
[2] C. Eberlein, Phys. Rev. Lett. **76**, 3842 (1996).
[3] N.E. Tran, S.G. Lambrakos, submitted for publication.
[4] J.R. Willison, Phys. Rev. Lett. **81**, 5430 (1998).
[5] R. Hiller *et al.*, Phys. Rev. Lett. **69**, 1182 (1992).
[6] B.P. Barber *et al.*, Phys. Rep. **281**, 65-143 (1997).
[7] T. Lepoint *et al.*, J. Acoust. Soc. Am. **101**, 2012 (1997).
[8] C.C. Wu and P.H. Roberts, Phys. Rev. Lett. **70**, 3424 (1993).
[9] W.C. Moss *et al.*, Phys. Fluids, **6**, 2979 (1994).
[10] D. A. McQuarrie, *Quantum chemistry* (University S.B, 1993), 5-11.
[11] S. Glasstone *et al.*, *Controlled Thermonuclear Reactions* (1960), 25-33.
[12] Y.B. Zel'dovich *et al.*, *Physics of Shock Waves and High-Temperature Hydrodynamic Phenomena* (1966), 111-122.
[13] C.E. Brennen, *Cavitation and Bubble Dynamics* (1995), 22
[14] M.P. Brenner, Rev. Mod. Phys. **74**, 425 (2002).
[15] N. Bach and R. Gilman, Actaphysico chim. **9**, 1 (1938).
[16] E.B Flint and K.S. Suslick, J. Phys. Chem. **95**, 1484 (1991).
[17] Y.I.Didenko *et al.*, Phys. Rev. Lett. **84**, 777 (2000).
[18] Y.I.Didenko *et al.*, Nature **407**, 877 (2000).
[19] D.J. Flannigan *et al.*, J. Organomet. Chem. **690**, 3513 (2005).